Non-Invasive Perfusion Imaging of the Human Brain via Breath-Holding: A DSC MRI Study

J.B. Schulman[1,2*], S. Kashyap[2], S.G. Kim[3,4], K. Uludağ[1,2,3,4*]

[1] Department of Medical Biophysics, University of Toronto, Toronto, ON, Canada

[2] Krembil Brain Institute, University Health Network, Toronto, ON, Canada

[3] Center for Neuroscience Imaging Research, Institute for Basic Science, Suwon, Republic of Korea

[4] Department of Biomedical Engineering, Sungkyunkwan University, Suwon, Republic of Korea

Correspondence:

Jacob Schulman

jacob.schulman@mail.utoronto.ca

Dr. Kamil Uludağ

Kamil.uludag@uhn.ca

Work Address:

Krembil Brain Institute

Toronto Western Hospital, University Health Network

399 Bathurst Street, Room 12MCL405

Toronto, Ontario, Canada M5T 2S8

Abstract

Dynamic susceptibility contrast (DSC) MRI plays a pivotal role in the accurate diagnosis and prognosis of several neurovascular diseases, but the technique's reliance on gadolinium, an intravascularly injected metal, presents a major limitation. Here, we determined the feasibility of using breath-holds to non-invasively induce DSC perfusion contrast. To achieve this, we acquired T_2*-weighted MRI data at both 3T and 7T from ten healthy participants who engaged in eight consecutive breath-holds (16 s each separated by 44 s of rest). By pairing a novel arterial input function with a standard DSC MRI analysis, we successfully quantified essential perfusion parameters, including the cerebral blood volume, flow, and transit delay, and found these perfusion values to be congruent with those documented in the literature using gadolinium. Breath-holding resulted in significantly higher contrast-to-noise (6.2 at 3T *vs* 8.5 at 7T) and gray matter-to-white matter contrast at higher field strength. For the first time, we have demonstrated the feasibility of DSC using breath-holds—we are confident that this method holds major

promise, both clinically and in research, effectively circumventing the need for invasive contrast agents, particularly at ultra-high field strength.

Keywords: MRI, Perfusion, DSC, Contrast, Deoxyhemoglobin

Introduction

Cerebral perfusion imaging allows clinicians to investigate diseases characterized by vascular abnormality, including atherosclerosis, cancer, and Moyamoya disease (Copen *et al.,* 2011; Harris *et al.,* 1998; Law *et al.,* 2008; Qiao *et al.,* 2016). Dynamic susceptibility contrast (DSC) MRI is a standard perfusion imaging technique wherein a bolus of paramagnetic contrast agent is tracked as it passes through the cerebral vasculature—the associated time course properties reflect underlying tissue perfusion in accordance with the principles of indicator dilution theory (Jahng *et al.,* 2014; Rosen *et al.,* 1990; Welker *et al.,* 2015; Zierler, 1962). DSC yields perfusion metrics possessing significant research and clinical utility, including the cerebral blood volume (*CBV*), cerebral blood flow (*CBF*), and mean transit time (*MTT*) (Copen *et al.,* 2011; Harris *et al.,* 1998; Law *et al.,* 2008; Qiao *et al.,* 2016; Tanaka *et al.,* 2011).

While gadolinium (Gd), an exogenous paramagnetic metal, is the standard contrast agent used clinically for DSC, researchers have recently exploited the paramagnetic properties of deoxyhemoglobin (dOHb) as an endogenous contrast alternative (Lee *et al.,* 2022; Poublanc *et al*., 2021; Sayin *et al.,* 2022; Schulman *et al.,* 2023; Vu *et al*., 2021; Vu *et al.,* 2023)—in essence, both Gd and dOHb induce T_2* signal changes that can be exploited in a DSC analysis. However, Gd is limited in that it is invasive, expensive, and exhibits toxicity in certain patient populations (Kanda, *et al.,* 2015; Rogowska *et al.,* 2018; Schlaudecker and Bernheisel, 2009). On the other hand, generating dOHb contrast has thus far relied on gas control systems that modify dOHb concentration in the blood through the induction of hypoxia (Lee *et al.,* 2022; Poublanc *et al*., 2021; Sayin *et al.,* 2022; Schulman *et al.,* 2023; Vu *et al*., 2021), hyperoxia (MacDonald *et al*., 2018), or hypercapnia (Vu *et al.,* 2023). Given the associated cost, set-up time, and expertise required for gas control system utilization, the widespread clinical implementation of dOHb contrast as an alternative to Gd is currently limited.

Unlike hypoxia and hyperoxia, hypercapnia (i.e., an increase in arterial CO_2) does not directly result in a change to the concentration of dOHb—rather, the CO_2 bolus induces a series of events which culminate in the transient rise of dOHb and *CBF* in the tissue through a process known as cerebrovascular reactivity (CVR) (Liu *et al.,* 2019). Given these inherent mechanistic differences, the use of hypercapnia for DSC relies on certain assumptions, including the constancy of oxygen metabolism, and most importantly, the presence of an arterial input function (AIF) which gains dispersion and delay as it passes through the tissue (see Discussion).

Physiologically, the effect of breath-holding is equivalent to that of hypercapnia induced by a gas control system (Bright *et al.,* 2011; Bright and Murphy, 2013; Liu *et al.,* 2019). However, there is no study that has developed and/or applied a DSC analysis pipeline to obtain perfusion information from signal changes induced by breath-holding. Thus, a breath-hold DSC (bhDSC) approach may provide, for the first time, DSC perfusion metrics without the use of Gd or a gas control system. To develop the bhDSC approach and test its feasibility, we acquired T_2*-weighted MRI data at 3T and 7T from ten healthy subjects who performed eight breath-holds (16 s each separated by 44 s of rest). In summary, bhDSC holds major

promise as a perfusion imaging alternative that circumvents the need for invasive contrast agents and expensive gas control system equipment.

Results

Gradient-echo 2D-EPI (GRE-EPI) imaging data were acquired on Siemens 3T Prisma and 7T Terra scanners from ten healthy subjects—each subject was scanned at both field strengths. The subjects were instructed to fixate on a countdown timer projected onto the back of the scanner, which indicated when to breathe regularly and when to perform a breath-hold. The first eight breath-hold "boluses" were averaged, wherein each bolus was allotted a 72 s window centered at the bolus maximum (Figure 1).

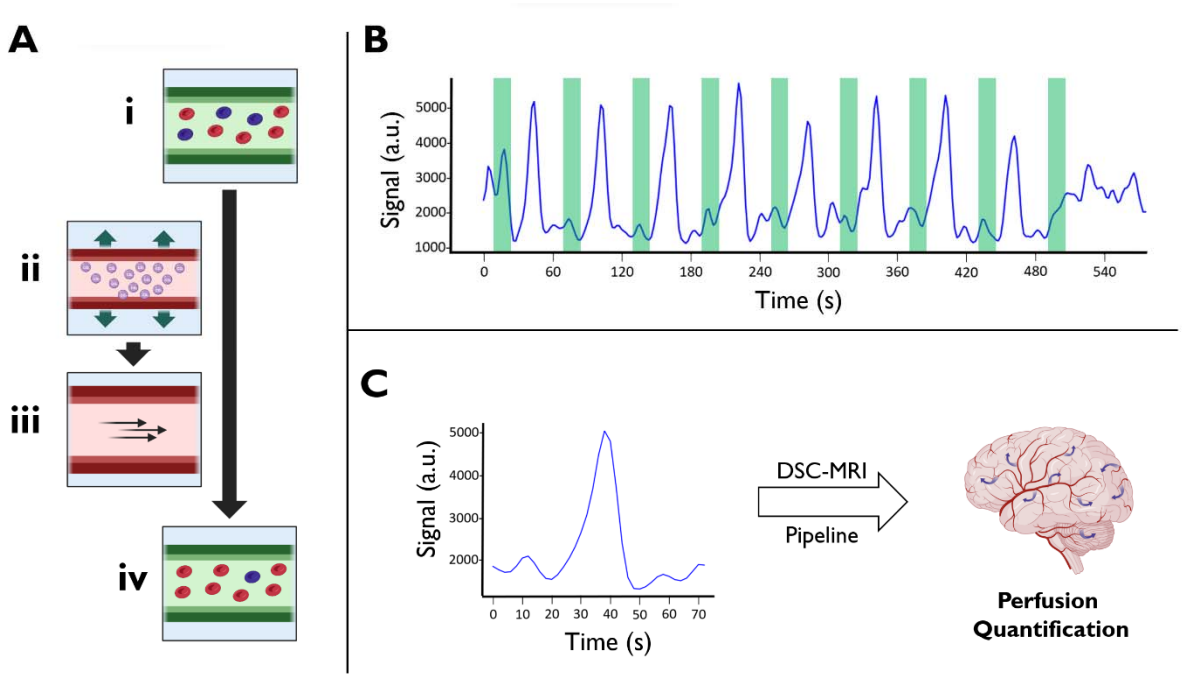

Figure 1. Summary of the Breath-hold Experiment. A. Description of the cerebrovascular reactivity phenomenon. At baseline, tissue blood oxygenation is roughly between 60-80% (**i**). Increased CO_2 from breath-holding causes vasodilation in the upstream arterial vasculature (**ii**), leading to increased blood flow (**iii**), and subsequently, a decrease in the downstream tissue dOHb concentration (**iv**), resulting in an MRI signal increase. **B.** Signal time course (blue) resulting from nine consecutive breath-holds (green) in a venous voxel. **C.** The signal time course resulting from the temporal average of the first eight boluses was then used for perfusion quantification.

Time Course Properties in bhDSC

The temporally averaged signal time courses were then converted to relaxation rate time courses ($\Delta R_2^*(t)$) by normalizing the time courses to the pre- and post- breath-hold baselines (see Methods).

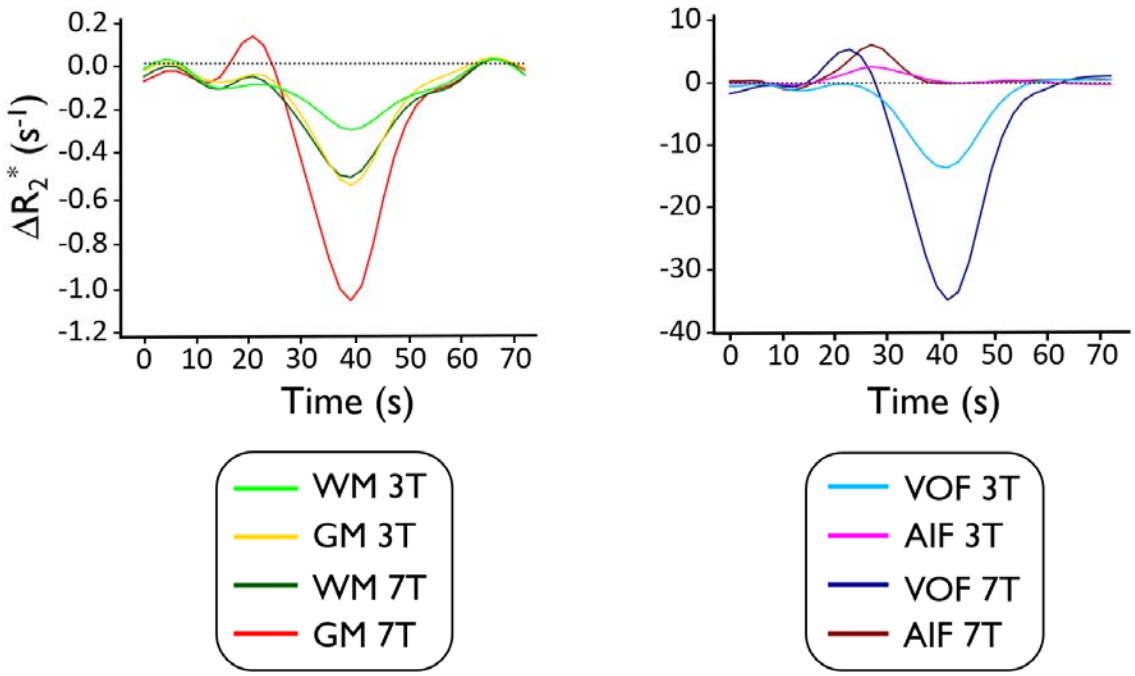

Figure 2. Breath-Hold-Induced Relaxation Rate Time Course Dynamics. Time courses were averaged across subjects for gray matter (GM), white matter (WM), vein (VOF), and artery (AIF) at 3T and 7T.

Figure 2 shows the breath-hold-induced ΔR_2* time courses averaged across all subjects, for arterial (AIF), venous (VOF), gray matter (GM), and white matter (WM) voxels at 3T and 7T. The ΔR_2*(t) bolus roughly follows the shape of a gamma variate function, with dispersion and delay increasing from input (AIF), to tissue (GM then WM), and ultimately to output (VOF), as is expected physiologically (Figure 2). Unlike the other time courses, the AIF has a positive ΔR_2* (to be discussed in Figure 4). This contrasts with Gd-DSC experiments where the ΔR_2*(t) in artery has the same sign as it does in GM, WM and vein. The bolus magnitude (defined here as the ΔR_2*(t) integral (*AUC*)) was found to be 1.5-2 times higher in GM relative to WM. Importantly, breath-holding at 7T resulted in larger bolus magnitudes in tissue (by ~2 times), artery (by ~2 times), and vein (by ~3 times) relative to 3T—this is also illustrated in the subject-wise data (Figure S1) and simulation results (Figure S2).

Breath-Hold CNR Properties

The contrast-to-noise ratio (*CNR*) and associated GM-to-WM contrast (ΔCNR) were subsequently quantified (see Methods for details). Although eight breath-holds were averaged in the main results of our work, we also studied the effect of averaging fewer breath-holds to determine whether shorter scan time (fewer breath-holds) would yield sufficient *CNR*.

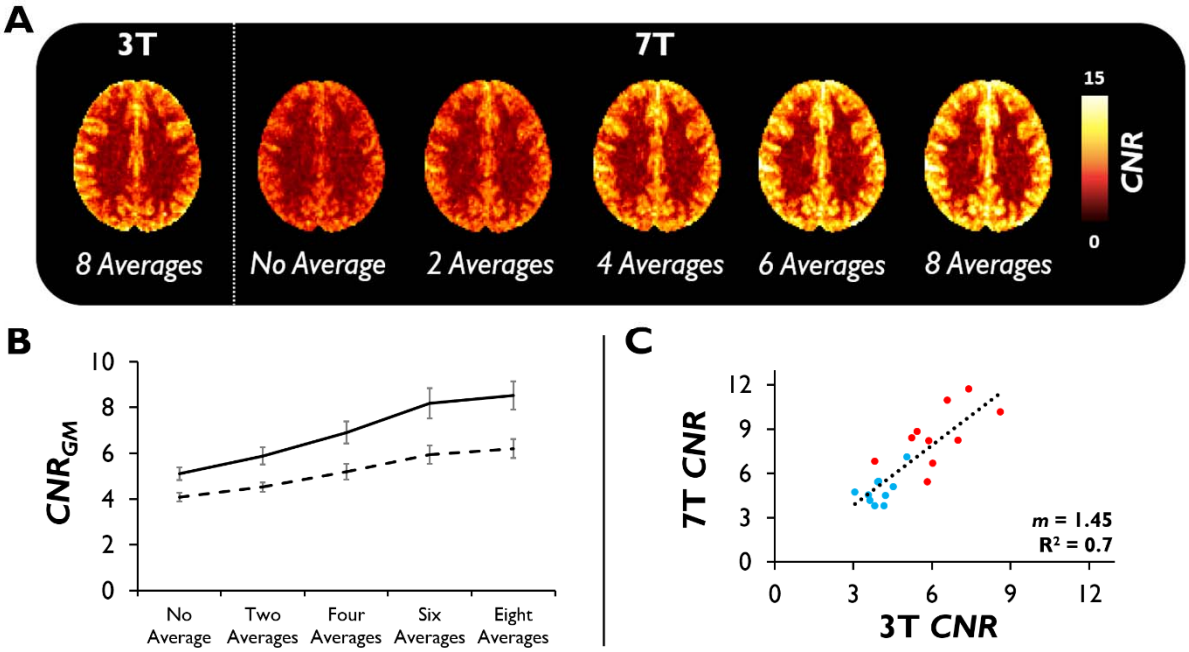

Figure 3. Breath-hold *CNR* Properties. A. *CNR* maps were calculated (Eq. 2), transformed to MNI152 2 mm anatomical space, and averaged across subjects for both 3T and 7T (axial view is slightly dorsal to the lateral ventricles). For illustration purposes, *CNR* maps are shown for no bolus averaging or 2, 4, 6, or 8 boluses averaged at 7T. **B.** Plot of subject-averaged CNR_{GM} at 3T (dashed) and 7T (solid) as a function of the number of breath-holds averaged (error bars represent the standard error). **C.** Linear regression of subject-wise GM (red) and WM (blue) *CNR* values at 3T *vs* 7T. *m* represents the regression slope.

Figure 3 shows the subject-averaged *CNR* at 3T and 7T when modifying the number of breath-holds averaged (Figure 3A and 3B), along with a subject-wise regression of GM and WM *CNR* values between 3T and 7T (Figure 3C). As more breath-holds were averaged, *CNR* increased significantly for both 3T (p = 0.00006) and 7T (p = 0.00007)—however, at both field strengths, we found the smallest gain in *CNR* when comparing 6 *vs* 8 breath-holds averaged (Figure 3B). *CNR* and ΔCNR were significantly higher at 7T relative to 3T (p_{CNR} = 0.0012; $p_{\Delta CNR}$ = 0.00075) (Table 1). In fact, 1 min of scan time at 7T resulted in the same *CNR* as 2 min 50 s of scan time at 3T and the same ΔCNR as 4 min 50 s of scan time at 3T. Of note, the subject-wise regression of *CNR* values between field strengths (Figure 3C), which provides some insight into subject repeatability, was very high (R^2 = 0.7)—according to the regression slope, *CNR* values were 1.45 times higher at 7T relative to 3T.

Novel Determination of an AIF for bhDSC

A prerequisite for DSC MRI is the presence of signal change at the arterial level, which is then used as an input function (i.e., AIF) for perfusion quantification in the tissue and veins. In Gd- or hypoxia-based methods, arterial signal change results from an increase in paramagnetic contrast agent in the artery, which subsequently passes through to the tissue (Rosen *et al.*, 1990; Zierler, 1962). However, given that blood oxygenation in healthy subjects is typically fully saturated in the major cerebral arteries, an increase in blood flow induced by CO_2 following breath-holding is not expected to significantly change the amount of dOHb in the arteries (Jain *et al.*, 2011; Severinghaus, 1979; Vestergaard and Larsson, 2019). Consequently, magnetic susceptibility in the arteries is not expected to change much as a result of breath-

holding. However, hypercapnia is known to result in arterial, capillary, and venous vasodilation (Liu *et al.*, 2019)—therefore, while MRI signal is not expected to change in the arteries from paramagnetic contrast agent, we expect that arterial vasodilation may result in a signal decrease, particularly at higher magnetic field strength (see Discussion). Thus, we developed a novel, alternative framework for selecting the AIF when using breath-holds (or hypercapnia in general).

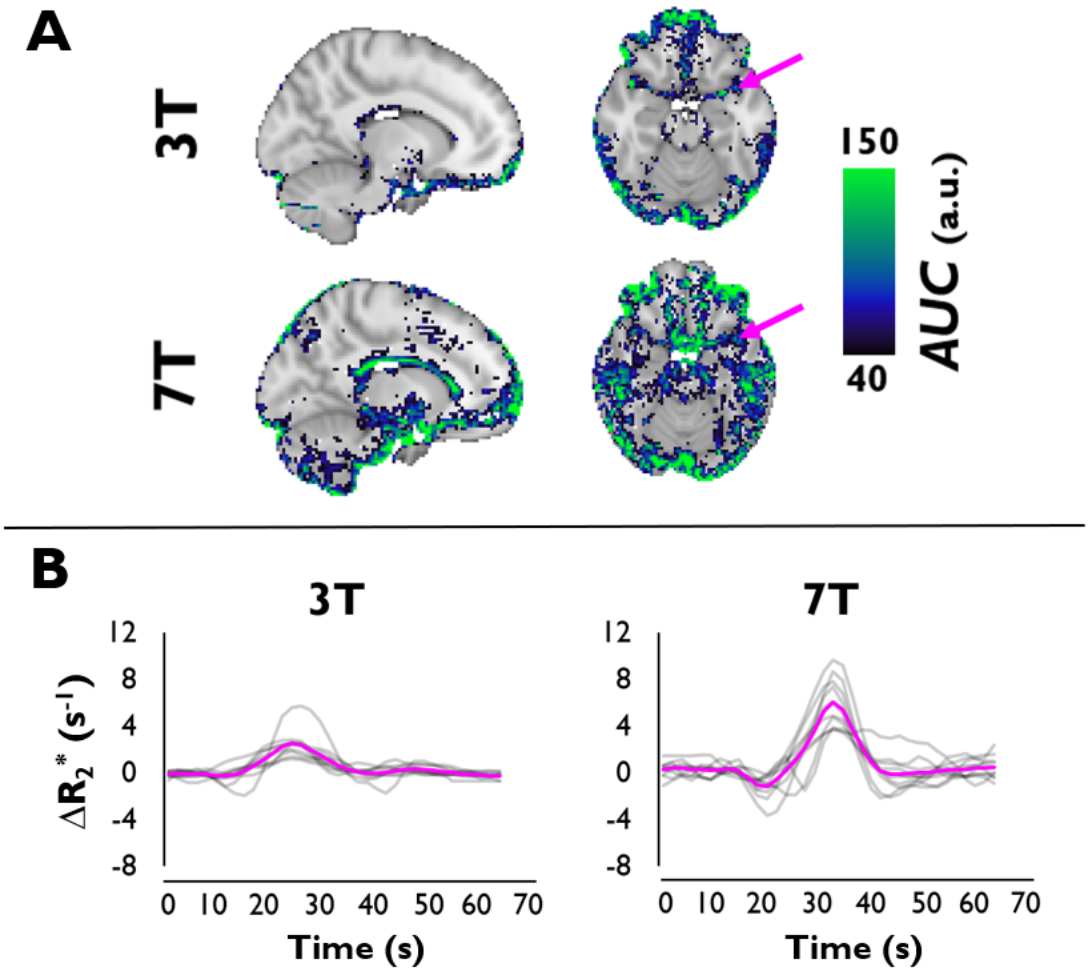

Figure 4. The AIF. A. ΔR_2^* *AUC* maps were calculated subject-wise, transformed to MNI152 2 mm anatomical space, and averaged at both 3T and 7T (sagittal and axial views are shown at the level of the middle cerebral artery). Pink arrows indicate an example of the AIF's location. *AUC* maps are overlaid onto the MNI152 2 mm anatomical template. **B.** The associated AIF ΔR_2^* time courses are shown at 3T and 7T, with subject-wise time courses in gray and subject-averaged time courses in pink.

Figure 4 shows voxels exhibiting a negative signal change (i.e., a positive relaxation change), and following averaging of these voxels in the middle cerebral artery (MCA), displays the subject-averaged AIF time courses at 3T and 7T in response to breath-holding. Voxels with a positive relaxation rate change are located adjacent to the ventricles and in regions containing/adjacent to veins or arteries—there are approximately two times more voxels fitting this criterion at 7T (Figure 4A), and the magnitude of the associated relaxation rate changes are significantly higher ($p < 0.0007$) in comparison to 3T. As a reminder, negative relaxation rate changes are observed in most cerebral territories (Figure 2). Thus, the presence of voxels displaying a positive relaxation rate change is, at first glance, counterintuitive given that the

predominant effect of breath-holding is a decrease in dOHb (i.e., decrease in the relaxation rate). However, when we simulated (Figure S2) a voxel containing a large vessel, with little-to-no change in dOHb in combination with vasodilation, a substantial relaxation rate increase was observed, and the magnitude of this increase was 4-5 times larger at 7T relative to 3T, in agreement with the experimental findings. Thus, the simulations and experimental results support the hypothesis that arterial vasodilation is responsible for the substantial relaxation rate increase observed in the arteries following breath-holding.

bhDSC Perfusion Quantification

The AIF was first scaled by the integral of the VOF, composed of voxels in the superior sagittal sinus (SSS)—this step was conducted as, like in tissue, the VOF integral is representative of the amount of contrast agent, whereas unlike in tissue, the AIF integral is representative of the degree of vasodilation. Following this scaling step, relative *CBV* (*rCBV*), *rCBF*, and *MTT* maps were calculated using a standard, truncated singular value decomposition (SVD) analysis, with an SVD noise threshold of 20% and hematocrit correction factor of 1.45 (Bjornerud and Emblem, 2010; Meier and Zierler, 1954; Østergaard *et al.*, 1996; Wirestam *et al.*, 2000; Schulman *et al.*, 2023).

		ΔS (%)		*CNR*		*ΔCNR*	*rCBV* (mL/100g)		*rCBF* (mL/100g/min)		*MTT* (s)
		GM	**WM**	**GM**	**WM**		**GM**	**WM**	**GM**	**WM**	**GM**
3T	**Mean**	**1.78**	**1.28**	**6.2**	**4.01**	**0.40**	**5.99**	**4.3**	**59.34**	**43.14**	**6.96**
	St.dev	*0.31*	*0.12*	*1.25*	*0.52*	*0.07*	*1.16*	*0.97*	*20.69*	*16.13*	*2.11*
	CV	0.17	0.09	0.20	0.13	0.17	0.19	0.23	0.35	0.37	0.30
7T	**Mean**	**2.2**	**1.27**	**8.52**	**4.8**	**0.51**	**5.2**	**3.3**	**44.29**	**25.48**	**7.36**
	St.dev	*0.41*	*0.23*	*1.87*	*0.94*	*0.12*	*2.15*	*1.39*	*10.05*	*6.05*	*2.52*
	CV	0.19	0.18	0.22	0.20	0.24	0.41	0.42	0.23	0.24	0.34

Table 1. Summary of bhDSC Perfusion Quantification Statistics. Average (mean), standard deviation (st.dev), and coefficient of variation (CV) values for 3T and 7T are shown.

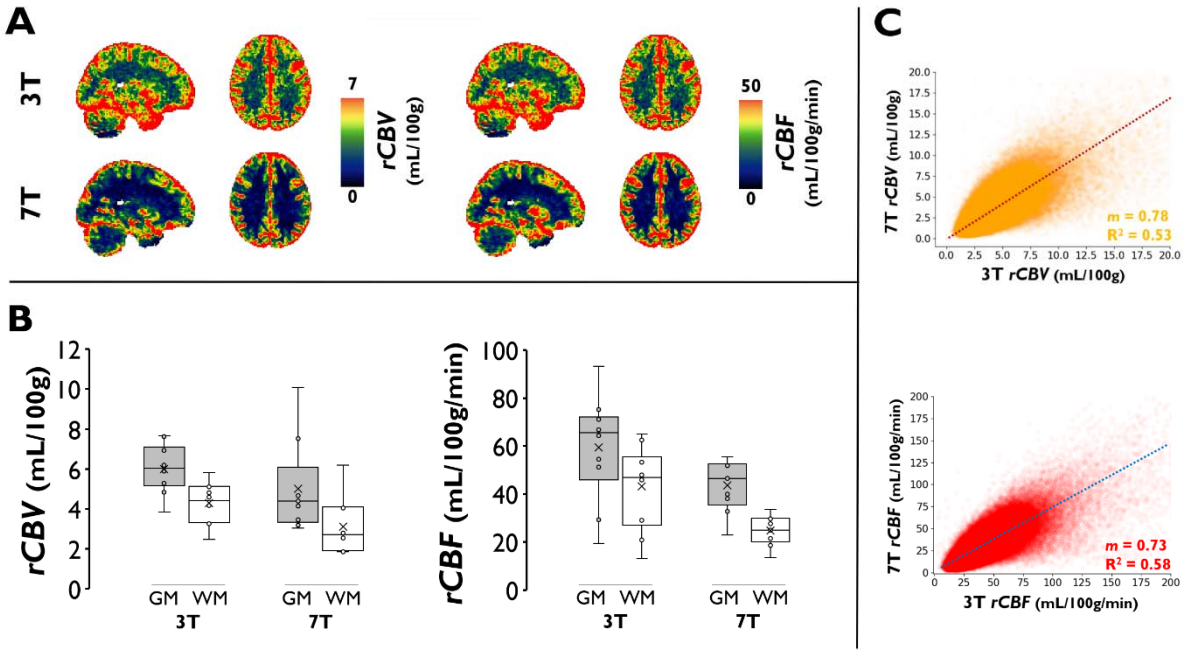

Figure 5. bhDSC Perfusion Quantification Results. A. *rCBV* (mL/100g) and *rCBF* (mL/100g/min) maps were calculated subject-wise, transformed to MNI152 2 mm anatomical space, and averaged at both 3T and 7T (sagittal and axial views are shown, slightly dorsal to lateral ventricles). **B.** Box and whisker plots show the calculated *rCBV* and *rCBF* (for GM and WM) at 3T and 7T. **C.** Voxel-wise regressions for *rCBV* and *rCBF* at 3T *vs* 7T. The regressions are based on voxels from the subject-averaged perfusion maps, and only voxels from the GM and WM are displayed (masks defined in Methods). Further masking was conducted to remove voxels at the periphery of the brain, where values differed substantially between 3T and 7T due to registration differences (i.e., in regions where the ratio of ΔS_{7T} to ΔS_{3T} was above the 95th percentile). Regressions are constrained such that the line of best fit intersects with the origin. *m* represents the regression slope.

Figure 5 shows the subject-averaged *rCBV* and *rCBF* perfusion maps (Figure 5A), subject-wise GM and WM perfusion values (Figure 5B), and voxel-wise regressions for *rCBV* and *rCBF* between 3T and 7T (Figure 5C). At 3T, *rCBV* values are slightly higher ($p = 0.108$) and *rCBF* values are significantly higher ($p = 0.0027$) than at 7T (Figure 5B). The attained GM-to-WM perfusion contrast (i.e., ratio of GM-to-WM perfusion values) was significantly higher at 7T relative to 3T for both *rCBF* ($p = 0.018$) and *rCBV* ($p = 0.016$) values. In addition, as shown in the subject-wise *rCBF* maps (Figure S3), GM-to-WM contrast is observed in all subjects at 7T, but not at 3T. A high coefficient of determination (voxel-wise $R^2 = 0.53$) is associated with the voxel-wise linear regression of 3T and 7T *rCBV* values—this is similarly the case for *rCBF* (voxel-wise $R^2 = 0.58$) (Figure 5C). Of note, *MTT* values in GM (Figure S4) are slightly higher, although not significantly ($p = 0.74$), at 7T as opposed to 3T ($MTT_{7T,GM} = 7.36 \pm 2.52$ *vs* $MTT_{3T,GM} = 6.96 \pm 2.11$)—due to low *CNR*, *MTT* values are not reported from the WM.

Delay Quantification

Finally, average bolus delay maps, relative to the AIF, were generated from the bhDSC data using a model-independent approach. First, the subject-wise relaxation rate time courses were transformed to MNI152 2 mm anatomical space and averaged across subjects. The average time courses were then interpolated to a temporal resolution of 0.5 s. The AIF time courses from each subject were time-shifted such that AIF bolus maximums were temporally aligned between subjects—these time courses were then

averaged. Finally, the subject-averaged AIF was shifted forward in 0.5 s steps, up to a maximum of 15 s, and the correlation between the AIF and tissue time course at each temporal shift was recorded. The temporal shift resulting in the highest correlation was determined to be the delay.

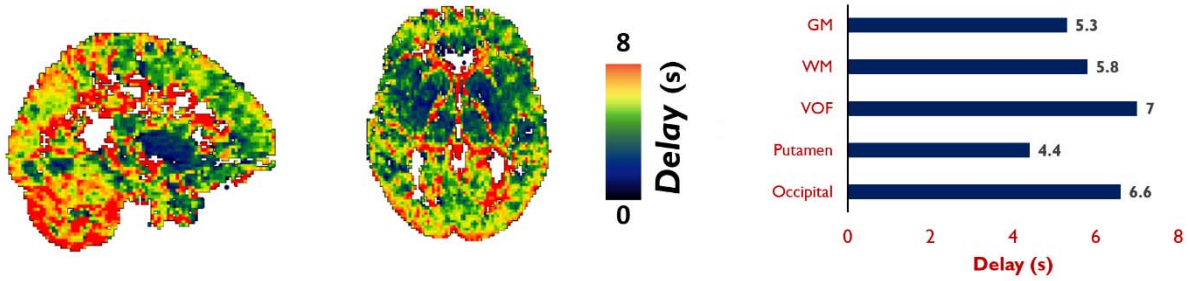

Figure 6. bhDSC Delay Map at 7T. Left. Tissue delay map relative to the AIF is shown in MNI152 2 mm anatomical space (sagittal and axial views are shown). **Right.** Calculated average delay values from various cerebral regions (note that the masks for the occipital GM and putamen are from the MNI structural atlas (Mazziotta *et al.*, 2001)).

Figure 6 shows the resulting, averaged bhDSC bolus delay map at 7T and the associated delay values across various cortical regions—results at 3T are also shown (Figure S5). Within the GM, subcortical regions such as the putamen yield a shorter delay (4.4 s) in comparison to average cortical GM (5.3 s), while the occipital lobe (perfused by the posterior cerebral artery) resulted in a longer delay (6.6 s). The perfusion output (VOF) of the brain was characterized by the longest (7 s) delay.

Discussion

We have shown, for the first time, that perfusion quantification is feasible using a breath-hold task, without exogenous contrast or additional equipment. To that end, we acquired T_2*-weighted data at 3T and 7T from ten healthy subjects who performed short-duration breath-holds (16 s each separated by 44 s of rest) and then analyzed the data using a DSC MRI framework to quantify perfusion. We have found the following:

- The AIF during a breath-hold is characterized by a negative signal change, likely representing vasodilation, as supported by both theory and the literature
- bhDSC-calculated *rCBV* and *rCBF* were within the physiological range of values reported in the literature using established perfusion MRI approaches and demonstrated strong voxel-wise linear agreement between 3T and 7T, with superior contrast at 7T
- While all subjects at 7T had observable GM-to-WM perfusion contrast, this was not the case at 3T
- At 7T, the breath-hold task yielded significantly higher *CNR* ($p = 0.0012$) and GM-to-WM contrast ($p = 0.00075$) relative to 3T
- *CNR* gains roughly plateau following approximately 5-to-6 min of scan time (averaging 5-6 breath-holds) at both 3T and 7T
- Bolus delay maps showed a clear delineation between various cortical regions, and the distribution of delay values across these territories agreed with those reported in the literature

From Breath-Hold to Signal Change

It has been well established that hypercapnia induced by breath-holding produces a quantifiable T_2* signal change in the tissue, which has been particularly useful in CVR and calibrated BOLD studies (Bright *et al.*, 2011; Bright and Murphy, 2013; Liu *et al.*, 2019). Of note, mild hypoxia is also known to accompany hypercapnia during breath-holding. However, given a roughly 0.65% reduction in arterial oxygen saturation during a 16 s breath-hold, the impact of breath-hold-induced hypoxia on T_2* signal change can be safely assumed to be negligible in comparison to the effect attributed to hypercapnia (Sasse *et al.*, 1996; Severinghaus, 1979).

It has long been known that increased P_aCO_2 (hypercapnia) leads to increased blood flow in the arteries, and ultimately, in tissue blood vessels and veins (Kety and Schmidt, 1948). This occurs either directly with CO_2 acting on the smooth muscle cells surrounding the artery/arterioles, or indirectly with CO_2 acting on the vascular endothelium, resulting in vasodilation and increased blood flow (Liu *et al.*, 2019). Therefore, a breath-hold, which results in a transient rise and fall (i.e., bolus) of P_aCO_2, is a relatively simple way to induce a transient bolus of *CBF*. Of note, the breath-hold duration has a roughly sigmoidal relationship with the resulting change in P_aCO_2 (Sasse et al., 1996), which has a roughly sigmoidal relationship with resulting change in *CBF* (Bhogal *et al.*, 2014). Given that oxygen metabolism is assumed to be constant during mild hypercapnia (Blockley *et al.*, 2013; Chen and Pike, 2010; Jain *et al.*, 2011; Vestergaard and Laarson, 2019, Zappe *et al.*, 2008), the *CBF* bolus resulting from arterial/arteriolar vasodilation now propagates to the tissue and permits the cerebral tissue to be supplied with more oxygen than it requires, leading to a transient surplus in oxygen, and thus, a reduction in dOHb.

The change in paramagnetic dOHb concentration is the basis for T_2* signal change in fMRI (Bandettini *et al.*, 1992; Kwong *et al.*, 1992; Ogawa *et al.*, 1990; Ogawa *et al.*, 1992). In the current study, we observed a roughly 10-15 s delay between the initiation of hypercapnia and the resulting T_2* signal change bolus onset (Figure 1), which is similarly observed in previous studies using CO_2 tasks—this delay has often been attributed to the time for CO_2 build-up in the lungs and the blood's lung-to-brain travel time (see references in Liu *et al.*, 2019). Ultimately, the decrease in dOHb results in a transient increase in MRI signal, and the magnitude of the signal change is dependent on the magnitude of ΔdOHb, field strength, pulse sequence, and tissue composition (Uludag *et al.*, 2009).

Determination of an AIF for bhDSC

To quantify *rCBV*, *rCBF*, and *MTT* using DSC MRI, the tissue bolus must be deconvolved with an input bolus from the artery (AIF) that acquires dispersion and delay as it enters the tissue, in accordance with indicator dilution theory (Rosen *et al.*, 1990; Zierler, 1962). While an AIF is expected and routinely determined when using Gd or hypoxia contrast, the presence of an AIF, along with its associated properties, are unknown in bhDSC—to address this, we examined the physiological processes underlying arterial signal change as a result of breath-holding.

As argued above, dOHb levels in healthy subjects do not change much in the arteries during breath-holding, given that there is effectively no oxygen exchange at this level of the vasculature and arterial blood oxygenation is already near-saturation (Jain *et al.*, 2011; Vestergaard and Larsson, 2019). Thus, given that most voxels in a typical T_2*-weighted MRI acquisition (2-4 mm voxel dimensions) likely consist of more than one tissue/vessel type, any observed signal increase in and around the MCA may represent signal changes from surrounding, early-perfused cortical tissue and nearby veins—using this as an AIF would violate basic tenets of indicator dilution theory.

Experimentally, we noticed that the MRI signal, which increased throughout most of the brain in response to a breath-hold, decreased in voxels containing major arteries and/or veins, particularly when adjacent to CSF, with a larger observed effect at 7T (Figure 4). To better understand this phenomenon, we modeled an arterial voxel with vasodilation (i.e., *CBV* change) but little to no dOHb change—in doing so, we found that vasodilation resulted in a sizeable signal decrease (i.e., relaxation rate increase) in accordance with our experimental findings, particularly at 7T (Figure S2). The reason for this phenomenon relies on the fact that the intravascular transverse relaxation rate is higher than the extravascular tissue and CSF relaxation rates at 7T, and to a lesser extent, at 3T (Uludag, 2009). Thus, an increase in *CBV* with little-to-no change in blood oxygenation leads to an MRI signal decrease. This signal origin has also been hypothesized as an explanation for the initial signal dip observed in fMRI studies (Uludag, 2010) and posited in other work (Jin and Kim, 2010). Although its magnitude depends on vessel orientation and voxel composition, measurable signal change is expected from our simulations to occur in any voxel where a large vessel increases in volume with negligible change in blood oxygenation, displacing extravascular tissue and/or CSF, particularly at 7T.

Our findings are also supported by the literature, where negative signal change during hypercapnia was found in and adjacent to the ventricles (Blockley *et al.*, 2011; Thomas *et al.*, 2013). At 3T, this effect results almost entirely from the difference between CSF and intravascular signal, as previously described (Thomas *et al.*, 2013). Voxels characterized by a signal decrease were observed in higher abundance at the arterial and venous level in a previous fMRI study at 7T (Bianciardi *et al.*, 2011), as is similarly observed in our study.

In sum, there is strong experimental and theoretical evidence that the positive relaxation rate change at the arterial level represents a time course of arterial vasodilation, in response to CO_2—this is not the case for Gd or hypoxia contrast where relaxation rate increases in the artery as direct consequence of increased paramagnetic contrast agent. Although it is not the traditional input of contrast agent-induced signal change, arterial vasodilation does in fact represent the input induced by hypercapnia from which downstream signal changes result. The careful selection and averaging of voxels in and around the MCA exhibiting this positive relaxation rate change provided us with a novel solution for deconvolving the tissue data with an input function. In fact, arterial signal change being opposite in sign to signal change observed in the majority of the brain will likely make it easier to identify an AIF in comparison to when using traditional DSC techniques.

CNR and bhDSC Perfusion Results

There is a significant increase in *AUC*, *CNR*, and GM-to-WM contrast (ΔCNR) as field strength increases (Figures 2 and 3; Table 1). These findings are supported by our simulations (Figure S2) and studies that have demonstrated a higher transverse relaxivity of dOHb as a function of field-strength (Blockley *et al.*, 2008; Kjolby *et al.*, 2009; Uludag *et al.*, 2009)—thus, for the same breath-hold duration and performance, higher signal change will be observed at 7T relative to 3T. This supports the notion that a bhDSC analysis will yield more robust and, hence, clinically valuable results at higher field strength.

There is also a significant increase in *CNR* as the number of breath-holds averaged increases, however, we found the smallest *CNR* and ΔCNR gains after approximately 5-6 breath-holds (Figures 3A and 3B). This suggests a saturation/plateau in *CNR* after approximately 5-to-6 min of scan time. Thus, in roughly the same amount of time that it takes to acquire a 2 mm isotropic arterial spin labeling (ASL) scan at 7T, the *CNR* is roughly 5-6 times higher when using the bhDSC technique (Ivanov *et al.*, 2017). Even a single

breath-hold at 7T—approximately 1 minute of scan time—provides roughly 2 times the *CNR* relative to previous studies that use gas control system-induced hypoxia at 3T (Poublanc *et al.*, 2021; Sayin *et al.*, 2023).

The subject-averaged *rCBV* and *rCBF* values and maps (Figures 4 and S3; Table 1) show sufficient GM-to-WM contrast and are generally within the documented range of previously reported values ($rCBV_{GM}$ = 3-11 mL/100g; $rCBF_{GM}$ = 52-137 mL/100g/min) (Bjornerud and Emblem, 2010; Carroll *et al.*, 2008; Knutsson *et al.*, 2010). However, while high GM-to-WM contrast is observed in all individual subject maps at 7T, this is not the case at 3T (Figure S3), suggesting that bhDSC will yield results of higher clinical import at higher field strength. Perfusion quantification likely differs between 3T and 7T because the *AUC* of tissue voxels and normalizing venous voxels scales differently as field strength increases (Figures 2 and S2)—in our study, the average AUC_{GM} roughly doubles while the average AUC_{VOF} nearly triples as field strength increases from 3T to 7T. In turn, this leads to lower calculated values of *rCBV* and *rCBF* at higher field strength. This observed scaling difference results from the non-linear intravascular contribution, which is a larger component of the signal at lower field strength (approximately 70-90% of the signal at 3T in comparison to roughly 0-10% of the signal at 7T in accordance with Uludag *et al.*, 2009). Regardless, there is a strong voxel-wise linear agreement/regression between 3T and 7T for both *rCBF* and *rCBV* (Figure 5C).

As previously mentioned, we do not consider *MTT* values in the WM to be reliable in bhDSC due to the low *CNR* in combination with the fact that *MTT* is calculated using already-noisy blood volume and flow information—thus the following discussion will focus on the GM. The MTT_{GM} values (Figure S4; Table 1) are twice as high as values obtained in studies using Gd contrast—however, the values in this study are similar to, if not lower than, those reported in studies using hypoxia contrast (Bjornerud and Emblem, 2010; Knutsson *et al.*, 2010; Schulman *et al.*, 2023; Vu *et al.*, 2021). This is expected as previous work has found longer bolus durations to result in higher calculated *MTT* values—a breath-hold of 16 s induces a roughly 35 s signal bolus, which is substantially longer than a Gd bolus (but similar in duration to a typical hypoxia bolus), and consequently yields a higher calculated *MTT* due to the inherent limitations of SVD (Schulman *et al.*, 2023). Although slightly higher at 7T, *MTT* quantification is not statistically different between field strengths. Of note, in accordance with the central volume principle (Meier and Zierler, 1954), the higher *MTT* values explain the slight underestimation of *rCBF* in comparison to average values reported in the literature (Bjornerud and Emblem, 2010; Carroll *et al.*, 2008; Knutsson *et al.*, 2010).

Finally, the delay maps are useful for addressing whether the breath-hold induces a bolus that traverses the cerebral vasculature in a sequential manner, acquiring delay/dispersion as it progresses. According to our delay maps (Figures 6 and S5), the bhDSC method yields delay values across the brain in accordance with the ordering of bolus arrival times reported in the literature when using Gd as a contrast agent (Ibaraki *et al.*, 2007). This provides strong evidence that bhDSC involves a bolus whose delay and dispersion properties are dependent on the location within the cerebral vascular network where tissue is perfused. Note that our 7T delay values are higher than those reported in Ibaraki *et al.* by approximately 4.5 s—this is because, when performing our delay analysis, each subject's AIF was shifted backward by 4.5 s on average, such that each subject's AIF was aligned with the earliest onset AIF prior to obtaining a subject-averaged time course (see Methods).

Clinical and Physiological Considerations for bhDSC

There are many benefits to the clinical implementation of our bhDSC method, including the lack of exogenous contrast, additional medical device equipment, and the limitations therein (i.e., patient discomfort, contrast agent extraversion, medical device maintenance, and additional costs) (Calamante, 2013; Poublanc *et al.*, 2021). Although the benefits are clear, it is important to consider whether there are physiological and/or physical processes, unique to breath-holding, which limit bhDSC's clinical utility in comparison to DSC acquired with Gd or hypoxia.

While vasodilation in the artery is the basis for bhDSC, additional vasodilation in the downstream tissue may confound the calculated perfusion metrics in bhDSC. In a standard DSC analysis (Østergaard *et al.*, 1996), it is assumed that *CBV* does not change, a condition which is fulfilled during mild hypoxia or Gd. To assess the degree to which tissue vasodilation confounds perfusion quantification, we simulated (see Schulman *et al.*, 2023 for framework) a 16 s breath-hold in addition to tissue vessel vasodilation and found moderate, global *rCBV* and *rCBF* underestimation (Figure S6). We found the underestimation to be almost identical in magnitude for voxels with differing vascular compositions and *CBV* values. As a result, the relative distributions of *rCBV* and *rCBF* throughout the brain are preserved as the voxels are scaled with roughly the same factor. That is, global underestimation does not confound the results when only relative values are considered, especially considering global quantification errors from other factors (i.e., AIF and VOF selection) override the effect from vasodilation. Thus, from our simulations, vasodilation in the tissue is not expected to confound relative bhDSC perfusion calculations. Nevertheless, introducing a scaling factor (i.e., derived from the simulations) that corrects for global estimation errors unique to bhDSC may be beneficial when comparing between other perfusion quantification methods.

Another consideration is the potential variability in the oxygen metabolism rate ($CMRO_2$) during breath-holding, as this would additionally violate an important DSC analysis assumption. There is very compelling evidence that shows a lack of significant $CMRO_2$ variability during mild hypercapnia or breath-holding, especially for the short, 16 s breath-hold duration employed in our study (Blockley *et al.*, 2013; Chen and Pike, 2010; Jain *et al.*, 2011; Vestergaard and Laarson, 2019; Zappe *et al.*, 2008).

Causality of flow in the vascular network is another important consideration. In healthy subjects, cerebral vasculature is assumed to respond similarly to a vasodilatory stimulus (Bhogal *et al.*, 2014; Fisher and Mikulis, 2021). However, in certain patients (i.e., those with steno-occlusive disease and/or vascular steal physiology), the affected arteries may have reduced vasodilatory capacity (Fisher and Mikulis, 2021), which would result in tissue downstream from the affected vessels yielding reduced calculated *CBV* values in comparison to tissue supplied by other vessels, even though the ground truth blood volume values may not be reduced. bhDSC could still be employed in these subjects, but caution should be taken to recognize that regions of apparent hypoperfusion relative to the rest of the brain may be a result of combined hypoperfusion and reduced vasodilatory capacity in the upstream vasculature.

As a final note, it is important to recognize that unlike Gd- and hypoxia-based methods, the signal change in bhDSC reflects an oxygen accumulation bolus that only begins at the tissue level—thus, signal change in bhDSC is capillary/venous dominated in comparison to other DSC methods where contrast agent-induced signal changes are observed in artery/arteriole as well. Thus, when comparing bhDSC with Gd-DSC perfusion results, there will likely be some incongruency in brain regions which have substantially more arterial blood—however, this difference may also provide an opportunity to combine information from multiple methods to isolate different blood pools.

Limitations and Future Directions

In comparison to Gd-based DSC, bhDSC has the inherent limitation of reduced *CNR* (by approximately 5 times at 3T). This stems from the fact that dOHb has a far lower molar susceptibility than Gd and the dOHb change following breath-holding is relatively small (Schulman *et al.*, 2023). However, as illustrated in this work, both the accuracy and precision of perfusion quantification with bhDSC is still sufficient on an individual subject level at 7T and on a group level at 3T. As well, physiological and physical noise correction methods, such as those based on multi-echo T_2* acquisition (Caballero-Gaudes and Reynolds, 2017), may enable bhDSC to yield robust perfusion metrics for individual subjects at lower field strength.

The breath-hold itself confers some limitations to the proposed method. Patient compliance during the repeated breath-holds of 16 s may be a somewhat difficult task for certain subjects, particularly the elderly and those with neurological disease (Jahanian *et al.*, 2017; Spano *et al.*, 2013). However, breath-holds are often applied in patients for body imaging, and as previously described, sufficient contrast can be obtained at 7T with fewer breath-holds, limiting the duration required for patient compliance. Another potential limitation is that motor activity associated with breath-holding can result in detectable motion during the scan—although, we found this to be minimal and easily corrected for using motion correction software in our study. Finally, there is inter-subject variability in the breath-holds, which is reflected in the variability of bolus shape and magnitude between subjects (Figure S1). However, the variability (i.e., coefficient of variation (CV)) of our calculated perfusion metrics (Table 1) is on par with that observed in a previous study (Vu *et al.*, 2021) which used a gas control system for DSC quantification at 3T ($rCBV_{CV}$ = 0.33; $rCBF_{CV}$ = 0.42), limiting the concern that the contrast bolus needs to be standardized across subjects to ensure precision of the calculated perfusion values. Regardless, precision should be enhanced in future work by optimizing the breath-hold approach—providing more detailed instructions to the subjects, including whether an end-inspiration or end-expiration is employed (Scouten and Schwarzbauer, 2008).

In the future, the clinical utility of the bhDSC technique must be validated in patients. It might also be sensible to experiment with the breath-hold duration—in previous work, it was determined that a 30 s or longer breath-hold would induce a near-maximal CO_2 stimulus, and thus, *CNR* (Sasse *et al.*, 1996). However, the breath-hold employed in this study balances patient tolerability and repeatability with optimal *CNR*, and it is advised that forthcoming studies employ a similar strategy when designing breath-hold paradigms for bhDSC. Finally, to provide more clinical centers with access to this method, it will be prudent to assess the viability of and optimize the bhDSC technique at lower field strengths.

Conclusion

For the first time, we used breath-hold-induced T_2*-MRI signal changes to quantify perfusion with DSC, at both 3T and 7T. This was made possible by developing and applying a novel arterial input function strategy, to be used specifically in breath-hold and hypercapnic paradigms. In doing so, we found that perfusion values (i.e., *rCBF* and *rCBV*) showed sufficient GM-to-WM contrast and were within the physiological range of expected values. We hope that the methods and results presented in this study will pave the way toward contrast-free perfusion imaging, both clinically and in research.

Methods

Subjects

This study was approved by the Research Ethics Board of Sungkyunkwan University and all procedures followed the principles expressed in the Declaration of Helsinki. Informed consent was obtained in all 10 healthy volunteers (age: 30.4 ± 9.4 years, 3 female). Please note that the same subjects were scanned at both 3T and 7T.

MRI Sequences and Experimental Protocols

MRI data were acquired at the Center for Neuroscience Imaging Research at Sungkyunkwan University on the Siemens 3T Prisma (Siemens Healthineers, Erlangen, Germany) and Siemens 7T Terra (Siemens Healthineers, Erlangen, Germany) using the commercially available 64 channel head/neck and 32 channel head coils (Nova Medical, Wilmington, USA).

Structural MRI

The 3T parameters were as follows: 3D-MP2RAGE (Marques *et al.*, 2010) with 1.0 mm isotropic spatial resolution (176 sagittal slices; GRAPPA = 3; Ref lines PE = 32; FoVread = 250 mm; phase-encoding = A-P; TI1/TI2 = 700/2500 ms; □1/□2 = 4°/5°; TE/TR = 2.98/5000 ms; bandwidth = 240 Hz/px; echo-spacing = 7.1 ms; TA = 8:22 min).

The 7T parameters were as follows: 3D-MP2RAGE (Marques *et al.* 2010) with 0.7 mm isotropic spatial resolution (240 sagittal slices; GRAPPA = 3; Ref lines PE = 36; FoVread = 224 mm; phase-encoding = A-P; TI1/TI2 = 1000/3200 ms; □1/□2 = 4°/4°; TE/TR = 2.29/4500 ms; partial-Fourier$_{slice}$ = 6/8; bandwidth = 200 Hz/px; echo-spacing = 7.3 ms; TA = 9:15 min).

Breath-hold MRI

The 3T parameters were as follows: Gradient-echo 2D-EPI (GRE-EPI) with 2.0 mm isotropic spatial resolution (64 interleaved axial slices; GRAPPA = 2; Ref lines PE = 46; SMS = 2; Ref. scan = EPI; FatSat = True; FoVread = 192 mm; phase-encoding = P-A; TE = 30 ms; □ = 70°; TR = 2000 ms; bandwidth = 2312 Hz/px; echo-spacing = 0.53 ms; EPI factor = 94) was acquired for the breath-hold experiment (260 TRs, TA = 8:53 min). 6 measurements of opposite phase-encoded (A-P) data were also acquired for susceptibility distortion correction.

The 7T parameters were as follows: GRE-EPI with 2.0 mm isotropic spatial resolution (74 interleaved axial slices; GRAPPA = 3; Ref lines PE = 54; SMS = 2; Ref. scan = EPI; partial-Fourier$_{phase}$ = 6/8; FatSat = True; FoVread = 192 mm; phase-encoding = P-A; TE = 20 ms; □ = 50°; TR = 2000 ms; bandwidth = 2368 Hz/px; echo-spacing = 0.53 ms; EPI factor = 96) was acquired for the breath-hold experiment (250 TRs, TA = 8:46 min). 6 measurements of opposite phase-encoded (A-P) data were also acquired for susceptibility distortion correction. Please note that the spatial resolution has **not** been optimized for 7T in this study—we have chosen the same spatial resolution as at 3T to allow for easier comparison.

For the breath-hold scans, subjects were instructed to fixate on a black cross at the center of an iso-luminant gray screen and a countdown timer which indicated when to breathe regularly and when to perform a breath-hold. Specifically, each breath-hold block was composed of three sections: 10 s of preparation with regular breathing, 16 s of breath-holding, and 34 s of regular breathing (Figure 1). This was repeated nine times to obtain multiple boluses for averaging, with an added final baseline of 80 s.

Only the first eight boluses were used for each subject as the response to the final breath-hold bolus was not fully included during the acquisition for some subjects.

Preprocessing

FSL (version 6.0.4), AFNI (version 23.0.07), and in-house Python scripts (see Code Availability) were used for image pre-processing (Cox, 1996; Jenkinson *et al.*, 2012). Anatomical and breath-hold T_2* data from both scanners were corrected for gradient nonlinearities using the Human Connectome Project's version of the gradunwarp tool (https://github.com/Washington-University/gradunwarp).

The MP2RAGE structural data were pre-processed using presurfer (https://github.com/srikash/presurfer) and skull-stripped using SynthStrip (Hoopes *et al.*, 2022). The background denoised T1-weighted UNI image was segmented using FSL FAST (Zhang *et al.*, 2001) to obtain three tissue classes corresponding to gray matter (GM), white matter (WM), and cerebrospinal fluid (CSF). The breath-hold data then underwent slice-timing (3dTshift, AFNI), motion (mcflirt, FSL), and distortion correction (topup, FSL) (Andersson *et al.*, 2003; Jenkinson *et al.*, 2002). The pre-processed data were linearly detrended and temporally filtered by averaging each signal time point with a 1x5 Gaussian kernel. The first eight breath-hold blocks were then averaged, wherein each of the eight "boluses" was allotted a 72 s window centered at the bolus maximum and averaged—an example of an original and averaged time course is shown in Figure 1. The percentage maximal signal change (ΔS) and ΔS-to-noise ratio, hereafter termed contrast-to-noise ratio (*CNR*), were then calculated from the bolus-averaged signal time course:

$$\Delta S = \frac{|S_{Max} - S_0|}{S_0} * 100 \quad (1)$$

$$CNR = \frac{|S_{Max} - S_0|}{\varepsilon_t} \quad (2)$$

In Eq. 1, S_0 is the average signal of ten temporal volumes before and after (roughly defined as the time that the signal returns to the average pre-bolus baseline) the bolus and S_{Max} is the maximum signal increase. The *CNR* is computed as shown in Eq. 2, where ε_t is the standard deviation of signal for ten temporal volumes before and after the selected bolus divided by S_0. *CNR* GM-to-WM contrast (ΔCNR) was also calculated as follows:

$$\Delta CNR = \frac{(CNR_{GM} - CNR_{WM})}{sCNR_{GM}} \quad (3)$$

Where CNR_{GM} and CNR_{WM} represent the mean GM and WM *CNR*, respectively, and $sCNR_{GM}$ represents the standard deviation of *CNR* in GM. *S(t)* was then converted to the change in transverse relaxation rate time course ($\Delta R_2^*(t)$):

$$\Delta R_2^*(t) = -\left(\frac{1}{TE}\right) * ln\left(\frac{S(t)}{S_0}\right) \quad (4)$$

The above equations were applied to T_2*-weighted breath-hold data from all subjects at 3T and 7T to generate ΔS, CNR, and $\Delta R_2^*(t)$ maps.

To facilitate group analyses, these maps, along with the later described perfusion maps, were transformed to FSL's MNI152 2 mm space. The processed bhDSC data were first registered to the subject's anatomical space (6 dof flirt, FSL) and the anatomical data were then non-linearly registered (fnirt, FSL) to the FSL MNI152 2 mm template (Jenkinson and Smith, 2001; Jenkinson *et al.*, 2012). The two transformation matrices were then combined into a subject-specific native-to-MNI space warp matrix and applied to all the subject-specific maps. The MNI space-transformed maps were then averaged across all subjects to generate mean $bhDSC_{3T}$ and $bhDSC_{7T}$ perfusion maps. Data were also subjected to visual quality control following each processing step.

Gray and White Matter Segmentation

GM and WM masks were generated, at both 3T and 7T, using whole-brain anatomical data (FSL FAST). The partial volume estimate maps were then thresholded at 0.9, binarized, and transformed from anatomical to GRE-EPI space for each subject (nearest-neighbor interpolation). Arterial and venous voxels were removed from the masks by thresholding the standard deviation map (only voxels with values in the lowest 10% of the ε_t range were kept in the mask) and using the output to mask the binarized FAST segmentations—the assumption being that voxels with high *CBV* have higher physiological noise due to pulsatility, leading to higher values of ε_t which can be removed from further analysis (Kashyap *et al.*, 2018; Schulman *et al.*, 2023). The whole-brain GM and WM masks were then applied to each subject's perfusion, ΔS, and *CNR* maps to obtain average GM and WM values (Table 1). GM and WM masks were also generated in standard space from the MNI152 T_1 2 mm template using the procedure described above.

Defining the AIF and VOF

In DSC MRI, it is critical to define an input function that is then used to normalize and deconvolve the tissue data—this input is defined at the level of the artery and is consequently termed the arterial input function (AIF) (Calamante *et al.*, 2013). Typically, to represent the AIF, 10-15 arterial voxels within or adjacent to the M1 segment of the middle cerebral artery (MCA) are identified, with ΔS values above the 95th percentile, and zero delay (see delay quantification below). However, given the spatial resolution of GRE-EPI (typically 2-4 mm in each dimension), signal change derived at the arterial level is likely contaminated by signal changes from cortical tissue and nearby veins. With this in mind, we developed an alternative, novel method to obtain an AIF from the breath-hold data, which can be used in any study that uses hypercapnia to calculate perfusion at high or ultra-high field strength. In essence, the selection criteria are the same as those described above, but voxels yielding **negative** Δ values, with magnitude above the 95th percentile (S_{Max} is replaced with S_{Min} in Eq. 1), were used instead. We hypothesize that the resulting signal time course reflects vasodilation at the arterial level in response to the CO_2 stimulus (see Results and Discussion).

In DSC MRI, it is also useful to define an output function from the cerebral draining veins, whose magnitude can be used to scale the measured AIF (Calamante *et al.*, 2013). Using both GRE-EPI and GRE-EPI-registered anatomical data, 10-15 venous voxels within or adjacent to the superior sagittal sinus (SSS), with ΔS values above the 99th percentile, long delay (~ 2-3 s), and low S_0 (as vein contains more dOHb than artery, reducing the baseline GRE signal) were defined and averaged. This averaged venous time course is hereafter termed the venous output function (VOF).

Perfusion Quantification

All voxel time courses were truncated to commence at the start of the AIF bolus and finish at the end of the VOF bolus. The AIF was then scaled by the integral of the VOF using the following equation:

$$AIF_{Scaled}(t) = \frac{\int_0^\infty VOF(t)dt}{\int_0^\infty AIF(t)dt} * AIF(t) \quad (5)$$

This step was conducted as, like in tissue, the VOF integral is representative of the amount of contrast agent (dOHb), whereas unlike in tissue, the AIF integral is representative of the degree of vasodilation. Relative cerebral blood volume (*rCBV*), relative cerebral blood flow (*rCBF)*, and mean transit time (*MTT)* maps were then calculated using a standard, truncated singular value decomposition (SVD) analysis, with an SVD noise threshold of 20% and hematocrit correction factor of 1.45 (Bjornerud and Emblem, 2010; Meier and Zierler, 1954; Østergaard *et al.*, 1996; Wirestam *et al.*, 2000; Schulman *et al.*, 2023). Note that these perfusion values are 'relative', not absolute; research has shown perfusion imaging values to depend on various contrast agent and acquisition parameters (Kiselev *et al.*, 2001; Schulman *et al.*, 2023).

Delay Quantification

Average bolus delay maps were also generated from the bhDSC data at 3T and 7T. Unlike the other perfusion metrics where DSC quantification was conducted in native space, the delay maps were calculated using the group average data.

First, the relaxation time courses were transformed to MNI152 2 mm anatomical space (using the previously described warp matrices) and averaged across subjects. The average time courses were then linearly interpolated to a temporal resolution of 0.5 s. The AIF time course from each subject was time-shifted backward to align with the bolus maximum of the earliest onset subject AIF (on average, roughly 4.5 s backward for 7T data and 10.5 s backward for 3T data)—these time courses were then averaged. The subject-averaged AIF was then shifted forward in 0.5 s steps, up to a maximum of 15 s, and the correlation between the AIF and tissue time courses for each voxel at each temporal shift was recorded. The temporal shift resulting in the highest correlation was determined to be the delay in a model-independent manner. A similar delay quantification method has been employed in previous studies using resting-state fMRI data (Khalil *et al.*, 2017; Lv *et al.*, 2013).

Note that the calculated delay maps reflect a combination of artery-to-tissue delay, tissue transit time, and dispersion, given that the AIF time courses were simply shifted to find the maximal correlation with each voxel time course (i.e., there was no separately modeled dispersion parameter in this analysis). The masks used for delay quantification in the occipital GM and putamen come from the MNI structural atlas (Mazziotta *et al.*, 2001).

Statistics

Parameters measured in native space have a calculated mean, standard deviation, and coefficient of variation (CV) for GM and WM, at both field strengths (Table 1). Note that CV is calculated as the inter-subject standard deviation divided by the parameter mean. Linear regressions were conducted for voxel-wise comparisons of *rCBV*, *rCBF*, and *MTT*, and subject-wise comparisons of *CNR*.

We found the data to be normally distributed for all measured parameters in GM and WM using the Shapiro-Wilk test. Thereafter, any statistical testing that was conducted for the experimental data (i.e., comparing mean GM and WM values at different field strengths) was done by applying a two-tailed paired student's t-test, with an alpha of 0.05.

Data and Code Availability

Anonymized subject data will be shared with any investigator for the purpose of ensuring reproducibility of the results presented in this work.

Analysis and simulation code will be **made available on GitHub and appended here** upon acceptance of the manuscript.

Conflict of Interest

The listed authors have no conflicts of interest to declare.

Author Contributions

J.B.S: Conceptualization, Data Curation, Formal Analysis, Investigation, Methodology, Software, Visualization, and Writing

S.K: Data Curation, Software, and Writing

S.G.K: Funding Acquisition, Resources, Supervision, and Writing

K.U: Conceptualization, Formal Analysis, Funding Acquisition, Investigation, Methodology, Project Administration, Resources, Supervision, and Writing

Funding

The research conducted in this paper was supported by funding from the Canadian Institutes of Health Research (CIHR) to K.U. The study was also supported by the Institute for Basic Science, Suwon, Republic of Korea (IBS-R015-D1) to S.G.K.

Acknowledgments

We would like to thank Boohee Choi and Suji Jeong at the Institute for Basic Science for helping us acquire the data. Figure 1 was created with BioRender.com.

References

Andersson, J.L.R., Skare, S., Ashburner, J., 2003. How to correct susceptibility distortions in spin-echo echo-planar images: application to diffusion tensor imaging. Neuroimage 20, 870–888. https://doi.org/10.1016/S1053-8119(03)00336-7

Aslan, S., Xu, F., Wang, P.L., Uh, J., Yezhuvath, U.S., van Osch, M., Lu, H., 2010. Estimation of labeling efficiency in pseudocontinuous arterial spin labeling. Magn Reson Med 63, 765–771. https://doi.org/10.1002/mrm.22245

Bandettini, P.A., Wong, E.C., Hinks, R.S., Tikofsky, R.S., Hyde, J.S., 1992. Time course EPI of human brain function during task activation. Magnetic Resonance in Medicine 25, 390–397. https://doi.org/10.1002/mrm.1910250220

Bhogal, A.A., Siero, J.C.W., Fisher, J.A., Froeling, M., Luijten, P., Philippens, M., Hoogduin, H., 2014. Investigating the non-linearity of the BOLD cerebrovascular reactivity response to targeted hypo/hypercapnia at 7T. NeuroImage 98, 296–305. https://doi.org/10.1016/j.neuroimage.2014.05.006

Bianciardi, M., Fukunaga, M., van Gelderen, P., de Zwart, J.A., Duyn, J.H., 2011. Negative BOLD-fMRI signals in large cerebral veins. J Cereb Blood Flow Metab 31, 401–412. https://doi.org/10.1038/jcbfm.2010.164

Bjørnerud, A., Emblem, K.E., 2010. A fully automated method for quantitative cerebral hemodynamic analysis using DSC–MRI. J Cereb Blood Flow Metab 30, 1066–1078. https://doi.org/10.1038/jcbfm.2010.4

Blockley, N. p., Jiang, L., Gardener, A. g., Ludman, C. n., Francis, S. t., Gowland, P. a., 2008. Field strength dependence of R1 and R relaxivities of human whole blood to prohance, vasovist, and deoxyhemoglobin. Magnetic Resonance in Medicine 60, 1313–1320. https://doi.org/10.1002/mrm.21792

Blockley, N.P., Driver, I.D., Francis, S.T., Fisher, J.A., Gowland, P.A., 2011. An improved method for acquiring cerebrovascular reactivity maps. Magn Reson Med 65, 1278–1286. https://doi.org/10.1002/mrm.22719

Blockley, N.P., Griffeth, V.E.M., Simon, A.B., Buxton, R.B., 2013. A review of calibrated blood oxygenation level-dependent (BOLD) methods for the measurement of task-induced changes in brain oxygen metabolism. NMR Biomed 26, 987–1003. https://doi.org/10.1002/nbm.2847

Bouten, J., Bourgois, J.G., Boone, J., 2020. Hold your breath: peripheral and cerebral oxygenation during dry static apnea. Eur J Appl Physiol 120, 2213–2222. https://doi.org/10.1007/s00421-020-04445-y

Bright, M.G., Donahue, M.J., Duyn, J.H., Jezzard, P., Bulte, D.P., 2011. The effect of basal vasodilation on hypercapnic and hypocapnic reactivity measured using magnetic resonance imaging. J Cereb Blood Flow Metab 31, 426–438. https://doi.org/10.1038/jcbfm.2010.187

Bright, M.G., Murphy, K., 2013. Reliable quantification of BOLD fMRI cerebrovascular reactivity despite poor breath-hold performance. Neuroimage 83, 559–568. https://doi.org/10.1016/j.neuroimage.2013.07.007

Bulte, D.P., Kelly, M., Germuska, M., Xie, J., Chappell, M.A., Okell, T.W., Bright, M.G., Jezzard, P., 2012. Quantitative measurement of cerebral physiology using respiratory-calibrated MRI. Neuroimage 60, 582–591. https://doi.org/10.1016/j.neuroimage.2011.12.017

Caballero-Gaudes, C., Reynolds, R.C., 2017. Methods for cleaning the BOLD fMRI signal. Neuroimage 154, 128–149. https://doi.org/10.1016/j.neuroimage.2016.12.018

Calamante, F., 2013. Arterial input function in perfusion MRI: a comprehensive review. Prog Nucl Magn Reson Spectrosc 74, 1–32. https://doi.org/10.1016/j.pnmrs.2013.04.002

Calamante, F., Gadian, D.G., Connelly, A., n.d. Delay and Dispersion Effects in Dynamic Susceptibility Contrast MRI: Simulations Using Singular Value Decomposition 8.

Carroll, T.J., Horowitz, S., Shin, W., Mouannes, J., Sawlani, R., Ali, S., Raizer, J., Futterer, S., 2008.

Quantification of Cerebral Perfusion Using the "Bookend Technique": an Evaluation in CNS Tumors. Magn Reson Imaging 26, 1352–1359. https://doi.org/10.1016/j.mri.2008.04.010

Cavuşoğlu, M., Pfeuffer, J., Uğurbil, K., Uludağ, K., 2009. Comparison of pulsed arterial spin labeling encoding schemes and absolute perfusion quantification. Magn Reson Imaging 27, 1039–1045. https://doi.org/10.1016/j.mri.2009.04.002

Chen, J.J., Pike, G.B., 2010. Global cerebral oxidative metabolism during hypercapnia and hypocapnia in humans: implications for BOLD fMRI. J Cereb Blood Flow Metab 30, 1094–1099. https://doi.org/10.1038/jcbfm.2010.42

Copen, W.A., Schaefer, P.W., Wu, O., 2011. MR Perfusion Imaging in Acute Ischemic Stroke. Neuroimaging Clin N Am 21, 259–283. https://doi.org/10.1016/j.nic.2011.02.007

Cox, R.W., 1996. AFNI: software for analysis and visualization of functional magnetic resonance neuroimages. Comput Biomed Res 29, 162–173. https://doi.org/10.1006/cbmr.1996.0014

De Vis, J.B., Hendrikse, J., Bhogal, A., Adams, A., Kappelle, L.J., Petersen, E.T., 2015. Age-related changes in brain hemodynamics; A calibrated MRI study. Hum Brain Mapp 36, 3973–3987. https://doi.org/10.1002/hbm.22891

Fisher, J.A., Mikulis, D.J., 2021. Cerebrovascular Reactivity: Purpose, Optimizing Methods, and Limitations to Interpretation – A Personal 20-Year Odyssey of (Re)searching. Frontiers in Physiology 12.

Gauthier, C.J., Madjar, C., Desjardins-Crépeau, L., Bellec, P., Bherer, L., Hoge, R.D., 2013. Age dependence of hemodynamic response characteristics in human functional magnetic resonance imaging. Neurobiol Aging 34, 1469–1485. https://doi.org/10.1016/j.neurobiolaging.2012.11.002

Harris, G.J., Lewis, R.F., Satlin, A., English, C.D., Scott, T.M., Yurgelun-Todd, D.A., Renshaw, P.F., 1998. Dynamic Susceptibility Contrast MR Imaging of Regional Cerebral Blood Volume in Alzheimer Disease: A Promising Alternative to Nuclear Medicine 6.

Hoopes, A., Mora, J.S., Dalca, A.V., Fischl, B., Hoffmann, M., 2022. SynthStrip: skull-stripping for any brain image. NeuroImage 260, 119474. https://doi.org/10.1016/j.neuroimage.2022.119474

Hornak, J., 2010. The basics of MRI.

Ibaraki, M., Ito, H., Shimosegawa, E., Toyoshima, H., Ishigame, K., Takahashi, K., Kanno, I., Miura, S., 2007. Cerebral Vascular Mean Transit Time in Healthy Humans: A Comparative Study with PET and Dynamic Susceptibility Contrast-Enhanced MRI. J Cereb Blood Flow Metab 27, 404–413. https://doi.org/10.1038/sj.jcbfm.9600337

Ivanov, D., Gardumi, A., Haast, R.A.M., Pfeuffer, J., Poser, B.A., Uludağ, K., 2017. Comparison of 3T and 7T ASL techniques for concurrent functional perfusion and BOLD studies. Neuroimage 156, 363–376. https://doi.org/10.1016/j.neuroimage.2017.05.038

Jahanian, H., Christen, T., Moseley, M.E., Pajewski, N.M., Wright, C.B., Tamura, M.K., Zaharchuk, G., 2017. Measuring vascular reactivity with resting-state blood oxygenation level-dependent (BOLD) signal fluctuations: A potential alternative to the breath-holding challenge? J Cereb Blood Flow Metab 37, 2526–2538. https://doi.org/10.1177/0271678X16670921

Jahng, G.-H., Li, K.-L., Ostergaard, L., Calamante, F., 2014. Perfusion Magnetic Resonance Imaging: A Comprehensive Update on Principles and Techniques. Korean J Radiol 15, 554–577. https://doi.org/10.3348/kjr.2014.15.5.554

Jain, V., Langham, M.C., Floyd, T.F., Jain, G., Magland, J.F., Wehrli, F.W., 2011. Rapid magnetic resonance measurement of global cerebral metabolic rate of oxygen consumption in humans during rest and hypercapnia. J Cereb Blood Flow Metab 31, 1504–1512. https://doi.org/10.1038/jcbfm.2011.34

Jenkinson, M., Bannister, P., Brady, M., Smith, S., 2002. Improved optimization for the robust and accurate linear registration and motion correction of brain images. Neuroimage 17, 825–841. https://doi.org/10.1016/s1053-8119(02)91132-8

Jenkinson, M., Beckmann, C.F., Behrens, T.E.J., Woolrich, M.W., Smith, S.M., 2012. FSL. Neuroimage 62,

782–790. https://doi.org/10.1016/j.neuroimage.2011.09.015
Jenkinson, M., Smith, S., 2001. A global optimisation method for robust affine registration of brain images. Med Image Anal 5, 143–156.
Jin, T., Kim, S.-G., 2010. Change of the cerebrospinal fluid volume during brain activation investigated by T(1rho)-weighted fMRI. Neuroimage 51, 1378–1383. https://doi.org/10.1016/j.neuroimage.2010.03.047
Kanda, T., Fukusato, T., Matsuda, M., Toyoda, K., Oba, H., Kotoku, J., Haruyama, T., Kitajima, K., Furui, S., 2015. Gadolinium-based Contrast Agent Accumulates in the Brain Even in Subjects without Severe Renal Dysfunction: Evaluation of Autopsy Brain Specimens with Inductively Coupled Plasma Mass Spectroscopy. Radiology 276, 228–232. https://doi.org/10.1148/radiol.2015142690
Kashyap, S., Ivanov, D., Havlicek, M., Poser, B.A., Uludağ, K., 2018. Impact of acquisition and analysis strategies on cortical depth-dependent fMRI. NeuroImage, Neuroimaging with Ultra-high Field MRI: Present and Future 168, 332–344. https://doi.org/10.1016/j.neuroimage.2017.05.022
Kety, S.S., Schmidt, C.F., 1948. THE EFFECTS OF ALTERED ARTERIAL TENSIONS OF CARBON DIOXIDE AND OXYGEN ON CEREBRAL BLOOD FLOW AND CEREBRAL OXYGEN CONSUMPTION OF NORMAL YOUNG MEN 1. J Clin Invest 27, 484–492.
Khalil, A.A., Ostwaldt, A.-C., Nierhaus, T., Ganeshan, R., Audebert, H.J., Villringer, K., Villringer, A., Fiebach, J.B., 2017. Relationship Between Changes in the Temporal Dynamics of the Blood-Oxygen-Level-Dependent Signal and Hypoperfusion in Acute Ischemic Stroke. Stroke 48, 925–931. https://doi.org/10.1161/STROKEAHA.116.015566
Kiselev, V. g., 2001. On the theoretical basis of perfusion measurements by dynamic susceptibility contrast MRI. Magnetic Resonance in Medicine 46, 1113–1122. https://doi.org/10.1002/mrm.1307
Kjølby, B.F., Mikkelsen, I.K., Pedersen, M., Østergaard, L., Kiselev, V.G., 2009. Analysis of partial volume effects on arterial input functions using gradient echo: a simulation study. Magn Reson Med 61, 1300–1309. https://doi.org/10.1002/mrm.21849
Knutsson, L., Ståhlberg, F., Wirestam, R., 2010. Absolute quantification of perfusion using dynamic susceptibility contrast MRI: pitfalls and possibilities. Magn Reson Mater Phy 23, 1–21. https://doi.org/10.1007/s10334-009-0190-2
Knutsson, L., Xu, X., Ståhlberg, F., Barker, P.B., Lind, E., Sundgren, P.C., van Zijl, P.C.M., Wirestam, R., 2017. Dynamic Susceptibility Contrast MRI at 7 T: Tail-Scaling Analysis and Inferences About Field Strength Dependence. Tomography 3, 74–78. https://doi.org/10.18383/j.tom.2017.00001
Kwong, K.K., Belliveau, J.W., Chesler, D.A., Goldberg, I.E., Weisskoff, R.M., Poncelet, B.P., Kennedy, D.N., Hoppel, B.E., Cohen, M.S., Turner, R., 1992. Dynamic magnetic resonance imaging of human brain activity during primary sensory stimulation. Proc Natl Acad Sci U S A 89, 5675–5679.
Law, M., Young, R.J., Babb, J.S., Peccerelli, N., Chheang, S., Gruber, M.L., Miller, D.C., Golfinos, J.G., Zagzag, D., Johnson, G., 2008. Gliomas: predicting time to progression or survival with cerebral blood volume measurements at dynamic susceptibility-weighted contrast-enhanced perfusion MR imaging. Radiology 247, 490–498. https://doi.org/10.1148/radiol.2472070898
Lee, D., Le, T.T., Im, G.H., Kim, S.-G., 2022. Whole-brain perfusion mapping in mice by dynamic BOLD MRI with transient hypoxia. J Cereb Blood Flow Metab 0271678X221117008. https://doi.org/10.1177/0271678X221117008
Liu, P., De Vis, J.B., Lu, H., 2019. Cerebrovascular reactivity (CVR) MRI with CO2 challenge: A technical review. Neuroimage 187, 104–115. https://doi.org/10.1016/j.neuroimage.2018.03.047
Lv, Y., Margulies, D.S., Cameron Craddock, R., Long, X., Winter, B., Gierhake, D., Endres, M., Villringer, K., Fiebach, J., Villringer, A., 2013. Identifying the perfusion deficit in acute stroke with resting-state functional magnetic resonance imaging. Ann Neurol 73, 136–140.

https://doi.org/10.1002/ana.23763
MacDonald ME, Berman AJL, Mazerolle EL, Williams RJ, Pike GB., 2018. Modeling hyperoxia-induced BOLD signal dynamics to estimate cerebral blood flow, volume and mean transit time. Neuroimage 178, 461-474. doi: 10.1016/j.neuroimage.2018.05.066.
Marques, J.P., Kober, T., Krueger, G., van der Zwaag, W., Van de Moortele, P.-F., Gruetter, R., 2010. MP2RAGE, a self bias-field corrected sequence for improved segmentation and T1-mapping at high field. Neuroimage 49, 1271–1281. https://doi.org/10.1016/j.neuroimage.2009.10.002
Mazziotta, J., Toga, A., Evans, A., Fox, P., Lancaster, J., Zilles, K., Woods, R., Paus, T., Simpson, G., Pike, B., Holmes, C., Collins, L., Thompson, P., MacDonald, D., Iacoboni, M., Schormann, T., Amunts, K., Palomero-Gallagher, N., Geyer, S., Parsons, L., Narr, K., Kabani, N., Le Goualher, G., Boomsma, D., Cannon, T., Kawashima, R., Mazoyer, B., 2001. A probabilistic atlas and reference system for the human brain: International Consortium for Brain Mapping (ICBM). Philos Trans R Soc Lond B Biol Sci 356, 1293–1322. https://doi.org/10.1098/rstb.2001.0915
Meier, P., Zierler, K.L., 1954. On the theory of the indicator-dilution method for measurement of blood flow and volume. J Appl Physiol 6, 731–744. https://doi.org/10.1152/jappl.1954.6.12.731
Ogawa, S., Lee, T.M., Kay, A.R., Tank, D.W., 1990. Brain magnetic resonance imaging with contrast dependent on blood oxygenation. Proc Natl Acad Sci U S A 87, 9868–9872.
Ogawa, S., Tank, D.W., Menon, R., Ellermann, J.M., Kim, S.G., Merkle, H., Ugurbil, K., 1992. Intrinsic signal changes accompanying sensory stimulation: functional brain mapping with magnetic resonance imaging. Proc Natl Acad Sci U S A 89, 5951–5955. https://doi.org/10.1073/pnas.89.13.5951
Ostergaard, L., Weisskoff, R.M., Chesler, D.A., Gyldensted, C., Rosen, B.R., 1996. High resolution measurement of cerebral blood flow using intravascular tracer bolus passages. Part I: Mathematical approach and statistical analysis. Magn Reson Med 36, 715–725. https://doi.org/10.1002/mrm.1910360510
Poublanc, J., Sobczyk, O., Shafi, R., Sayin, E.S., Schulman, J., Duffin, J., Uludag, K., Wood, J.C., Vu, C., Dharmakumar, R., Fisher, J.A., Mikulis, D.J., n.d. Perfusion MRI using endogenous deoxyhemoglobin as a contrast agent: Preliminary data. Magnetic Resonance in Medicine n/a. https://doi.org/10.1002/mrm.28974
Qiao, P.-G., Han, C., Zuo, Z.-W., Wang, Y.-T., Pfeuffer, J., Duan, L., Qian, T., Li, G.-J., 2017. Clinical assessment of cerebral hemodynamics in Moyamoya disease via multiple inversion time arterial spin labeling and dynamic susceptibility contrast-magnetic resonance imaging: A comparative study. Journal of Neuroradiology 44, 273–280. https://doi.org/10.1016/j.neurad.2016.12.006
Rogowska, J., Olkowska, E., Ratajczyk, W., Wolska, L., 2018. Gadolinium as a new emerging contaminant of aquatic environments. Environ Toxicol Chem 37, 1523–1534. https://doi.org/10.1002/etc.4116
Rosen, B.R., Belliveau, J.W., Vevea, J.M., Brady, T.J., 1990. Perfusion imaging with NMR contrast agents. Magn Reson Med 14, 249–265. https://doi.org/10.1002/mrm.1910140211
Sasse, S.A., Berry, R.B., Nguyen, T.K., Light, R.W., Mahutte, C.K., 1996. Arterial blood gas changes during breath-holding from functional residual capacity. Chest 110, 958–964. https://doi.org/10.1378/chest.110.4.958
Sayin, E.S., Schulman, J., Poublanc, J., Levine, H.T., Raghavan, L.V., Uludag, K., Duffin, J., Fisher, J.A., Mikulis, D.J., Sobczyk, O., 2023. Investigations of hypoxia-induced deoxyhemoglobin as a contrast agent for cerebral perfusion imaging. Hum Brain Mapp 44, 1019–1029. https://doi.org/10.1002/hbm.26131
Schlaudecker, J.D., Bernheisel, C.R., 2009. Gadolinium-associated nephrogenic systemic fibrosis. Am Fam Physician 80, 711–714.
Schulman, J.B., Sayin, E.S., Poublanc, J., Manalac, A., Fisher, J.A., Sobczyk, O., Duffin, J., Levine, H., Mikulis, D.J., Uludag, K., 2022. Deoxyhemoglobin versus gadolinium as contrast in dynamic

susceptibility perfusion imaging: simulations and scan validations. Proc Intl Soc Mag Reson Med 30, 337.

Schulman, J.B., Sayin, E.S., Manalac, A., Poublanc, J., Sobczyk, O., Duffin, J., Fisher, J.A., Mikulis, D., Uludağ, K., 2023. DSC MRI in the human brain using deoxyhemoglobin and gadolinium—Simulations and validations at 3T. Frontiers in Neuroimaging 2.

Scouten, A., Schwarzbauer, C., 2008. Paced respiration with end-expiration technique offers superior BOLD signal repeatability for breath-hold studies. Neuroimage 43, 250–257. https://doi.org/10.1016/j.neuroimage.2008.03.052

Severinghaus, J.W., 1979. Simple, accurate equations for human blood O2 dissociation computations. J Appl Physiol Respir Environ Exerc Physiol 46, 599–602. https://doi.org/10.1152/jappl.1979.46.3.599

Spano, V.R., Mandell, D.M., Poublanc, J., Sam, K., Battisti-Charbonney, A., Pucci, O., Han, J.S., Crawley, A.P., Fisher, J.A., Mikulis, D.J., 2013. CO2 blood oxygen level-dependent MR mapping of cerebrovascular reserve in a clinical population: safety, tolerability, and technical feasibility. Radiology 266, 592–598. https://doi.org/10.1148/radiol.12112795

Tanaka, Y., Nagaoka, T., Nair, G., Ohno, K., Duong, T.Q., 2011. Arterial spin labeling and dynamic susceptibility contrast CBF MRI in postischemic hyperperfusion, hypercapnia, and after mannitol injection. J Cereb Blood Flow Metab 31, 1403–1411. https://doi.org/10.1038/jcbfm.2010.228

Thomas, B.P., Liu, P., Aslan, S., King, K.S., van Osch, M.J.P., Lu, H., 2013. Physiologic underpinnings of negative BOLD cerebrovascular reactivity in brain ventricles. Neuroimage 83, 505–512. https://doi.org/10.1016/j.neuroimage.2013.07.005

Uludağ, K., Müller-Bierl, B., Uğurbil, K., 2009. An integrative model for neuronal activity-induced signal changes for gradient and spin echo functional imaging. NeuroImage 48, 150–165. https://doi.org/10.1016/j.neuroimage.2009.05.051

Uludağ, K., 2010. To dip or not to dip: Reconciling optical imaging and fMRI data. Proceedings of the National Academy of Sciences of the United States of America 107, E23. https://doi.org/10.1073/pnas.0914194107

Vestergaard, M.B., Larsson, H.B., 2019. Cerebral metabolism and vascular reactivity during breath-hold and hypoxic challenge in freedivers and healthy controls. J Cereb Blood Flow Metab 39, 834–848. https://doi.org/10.1177/0271678X17737909

Vu, C., Chai, Y., Coloigner, J., Nederveen, A.J., Borzage, M., Bush, A., Wood, J.C., 2021. Quantitative perfusion mapping with induced transient hypoxia using BOLD MRI. Magn Reson Med 85, 168–181. https://doi.org/10.1002/mrm.28422

Vu, C., Xu, B., González-Zacarías, C., Shen, J., Baas, K., Choi, S., Nederveen, A., Wood, J., 2023. Sinusoidal CO2 respiratory challenge for concurrent perfusion and cerebrovascular reactivity MRI. Frontiers in Physiology 14. https://doi.org/10.3389/fphys.2023.1102983

Welker, K., Boxerman, J., Kalnin, A., Kaufmann, T., Shiroishi, M., Wintermark, M., American Society of Functional Neuroradiology MR Perfusion Standards and Practice Subcommittee of the ASFNR Clinical Practice Committee, 2015. ASFNR recommendations for clinical performance of MR dynamic susceptibility contrast perfusion imaging of the brain. AJNR Am J Neuroradiol 36, E41-51. https://doi.org/10.3174/ajnr.A4341

Wirestam, R., Andersson, L., Ostergaard, L., Bolling, M., Aunola, J.P., Lindgren, A., Geijer, B., Holtås, S., Ståhlberg, F., 2000. Assessment of regional cerebral blood flow by dynamic susceptibility contrast MRI using different deconvolution techniques. Magn Reson Med 43, 691–700. https://doi.org/10.1002/(sici)1522-2594(200005)43:5<691::aid-mrm11>3.0.co;2-b

Zappe, A.C., Uludağ, K., Oeltermann, A., Uğurbil, K., Logothetis, N.K., 2008. The influence of moderate hypercapnia on neural activity in the anesthetized nonhuman primate. Cereb Cortex 18, 2666–2673. https://doi.org/10.1093/cercor/bhn023

Zhang, Y., Brady, M., Smith, S., 2001. Segmentation of brain MR images through a hidden Markov

random field model and the expectation-maximization algorithm. IEEE Trans Med Imaging 20, 45–57. https://doi.org/10.1109/42.906424
Zierler, K.L., 1962. Theoretical Basis of Indicator-Dilution Methods For Measuring Flow and Volume. Circulation Research 10, 393–407. https://doi.org/10.1161/01.RES.10.3.393

Figure Captions

Figure 1. Summary of the Breath-hold Experiment. A. Description of the cerebrovascular reactivity phenomenon. At baseline, tissue blood oxygenation is roughly between 60-80% (**i**). Increased CO_2 from breath-holding causes vasodilation in the upstream arterial vasculature (**ii**), leading to increased blood flow (**iii**), and subsequently, a decrease in the downstream tissue dOHb concentration (**iv**), resulting in an MRI signal increase. **B.** Signal time course (blue) resulting from nine consecutive breath-holds (green) in a venous voxel. **C.** The signal time course resulting from the temporal average of the first eight boluses was then used for perfusion quantification.

Figure 2. Breath-Hold-Induced Relaxation Rate Time Course Dynamics. Time courses were averaged across subjects for gray matter (GM), white matter (WM), vein (VOF), and artery (AIF) at 3T and 7T.

Figure 3. Breath-hold *CNR* Properties. A. *CNR* maps were calculated (Eq. 2), transformed to MNI152 2 mm anatomical space, and averaged across subjects for both 3T and 7T (axial view is slightly dorsal to the lateral ventricles). For illustration purposes, *CNR* maps are shown for no bolus averaging or 2, 4, 6, or 8 boluses averaged at 7T. **B.** Plot of subject-averaged CNR_{GM} at 3T (dashed) and 7T (solid) as a function of the number of breath-holds averaged (error bars represent the standard error). **C.** Linear regression of subject-wise GM (red) and WM (blue) *CNR* values at 3T *vs* 7T. *m* represents the regression slope.

Figure 4. The AIF. A. ΔR_2^* *AUC* maps were calculated subject-wise, transformed to MNI152 2 mm anatomical space, and averaged at both 3T and 7T (sagittal and axial views are shown at the level of the middle cerebral artery). Pink arrows indicate an example of the AIF's location. *AUC* maps are overlaid onto the MNI152 2 mm anatomical template. **B.** The associated AIF ΔR_2^* time courses are shown at 3T and 7T, with subject-wise time courses in gray and subject-averaged time courses in pink.

Figure 5. bhDSC Perfusion Quantification Results. A. *rCBV* (mL/100g) and *rCBF* (mL/100g/min) maps were calculated subject-wise, transformed to MNI152 2 mm anatomical space, and averaged at both 3T and 7T (sagittal and axial views are shown, slightly dorsal to lateral ventricles). **B.** Box and whisker plots show the calculated *rCBV* and *rCBF* (for GM and WM) at 3T and 7T. **C.** Voxel-wise regressions for *rCBV* and *rCBF* at 3T *vs* 7T. The regressions are based on voxels from the subject-averaged perfusion maps, and only voxels from the GM and WM are displayed (masks defined in Methods). Further masking was conducted to remove voxels at the periphery of the brain, where ΔS values differed substantially between 3T and 7T due to registration differences (i.e., in regions where the ratio of ΔS_{7T} to ΔS_{3T} was above the 95th percentile). Regressions are constrained such that the line of best fit intersects with the origin. *m* represents the regression slope.

Figure 6. bhDSC Delay Map at 7T. Left. Tissue delay map relative to the AIF is shown in MNI152 2 mm anatomical space (sagittal and axial views are shown). **Right.** Calculated average delay values from various cerebral regions (note that the masks for the occipital GM and putamen are from the MNI structural atlas (Mazziotta *et al.*, 2001)).

Tables

Table 1. Summary of bhDSC Perfusion Quantification Statistics. Average (mean), standard deviation (st.dev), and coefficient of variation (CV) values for 3T and 7T are shown.

		ΔS (%)		*CNR*		*ΔCNR*	*rCBV* (mL/100g)		*rCBF* (mL/100g/min)		*MTT* (s)
		GM	**WM**	**GM**	**WM**		**GM**	**WM**	**GM**	**WM**	**GM**
3T	**Mean**	**1.78**	**1.28**	**6.2**	**4.01**	**0.40**	**5.99**	**4.3**	**59.34**	**43.14**	**6.96**
	St.dev	*0.31*	*0.12*	*1.25*	*0.52*	*0.07*	*1.16*	*0.97*	*20.69*	*16.13*	*2.11*
	CV	0.17	0.09	0.20	0.13	0.17	0.19	0.23	0.35	0.37	0.30
7T	**Mean**	**2.2**	**1.27**	**8.52**	**4.8**	**0.51**	**5.2**	**3.3**	**44.29**	**25.48**	**7.36**
	St.dev	*0.41*	*0.23*	*1.87*	*0.94*	*0.12*	*2.15*	*1.39*	*10.05*	*6.05*	*2.52*
	CV	0.19	0.18	0.22	0.20	0.24	0.41	0.42	0.23	0.24	0.34